Received: 29 April 2025 | Revised: 27 May 2025 | Accepted: 10 June 2025

DOI: 10.1111/ijac.70011

SPECIAL ISSUE ARTICLE

# Electrochemical reduction-induced phase transformation and lattice modification in cubic zirconia (8YSZ)

**Christian Bechteler** | **Richard I. Todd**

Department of Materials, University of Oxford, Oxford, UK

**Correspondence**
Richard I. Todd, University of Oxford, Department of Materials, Parks Road, Oxford OX1 3PH, UK.
Email: richard.todd@materials.ox.ac.uk

**Funding information**
Engineering and Physical Sciences Research Council, Grant/Award Number: EP/T517811/1; Studienstiftung des deutschen Volkes—German Academic Scholarship Foundation; Henry Royce Institute, Grant/Award Number: EP/R010145/1

**Abstract**

This study investigates the effects of electrical loading on cubic 8YSZ (8 mol% yttria-stabilized zirconia) under different atmospheric conditions with a focus on electrical and structural changes, lattice modifications, and the formation of new phases. Upon applying an electric field during various atmospheric transitions from oxygen to air to argon or nitrogen, an increase in oxygen extraction and enhanced electrical conductivity was linked to the formation of an atmosphere-dependent defective FCC rocksalt phase, ZrO in Ar, and Zr(O,N) in nitrogen, as confirmed by EDS, X-ray diffraction, and Raman spectroscopy, with lattice parameters consistent at approximately 0.458 nm. The microstructure of the electrically loaded material showed elongated precipitates of this new phase, particularly along grain boundaries, which were a few tens to hundreds of nanometers in size. Furthermore, dopant segregation and microstructural instability due to this lattice modification and phase transformation were observed. Comparison to the behavior of tetragonal 3YSZ revealed significant differences between the two compositions. These findings highlight the role of electrochemical reduction in altering material properties, with potential implications for flash sintering and energy applications like solid oxide fuel and electrolyzer cells.

**KEYWORDS**

8YSZ, electrochemical reduction, flash sintering, lattice modification, phase transformation, stabilized zirconia, zirconium oxynitride

## 1 | INTRODUCTION

Electrochemical reduction of yttria-stabilized zirconia (YSZ) under an applied electric field at temperatures of several hundred degrees, which are conditions where solid oxide fuel cells (SOFC) or flash sintering (FS) operate, is a mechanism that has been investigated for more than 40 years. One phenomenon that is well known in the context of the electrochemical reduction of YSZ is graying or blackening of the usually white material due to the extraction of oxygen anions from the lattice,[1–6] which is usually attributed to removal of oxygen from the fluorite-based lattice of $ZrO_2$.

Recently, however, the possibility of a phase transformation in mainly cubic 8YSZ (8 mol% yttria-stabilized zirconia) during electrical loading has been reported during in situ synchrotron experiments by Charalambous et al.[7] In their DC tests, new peaks arose that are

consistent with a cubic F Bravais lattice. Based on a report by Schönberg from the 1950s,[8] in which the existence of FCC rocksalt ZrO was claimed, Charalambous et al. suggested the novel phase being FCC rocksalt ZrO with a lattice parameter of 0.46 nm. After the field was turned off at elevated furnace temperatures, the new diffraction peaks disappeared, so no further characterization of this phase was possible.[7]

In a follow-up investigation, Charalambous et al. reported the formation of nanopores and microstrains along the grain boundaries of 8YSZ,[7,9] leading to cracking along the grain boundaries, which agrees with observations by Dong and Chen,[10] who reported such a phenomenon for 8YSZ electrically loaded in Ar or 5%$H_2$/95%Ar. The phase field simulations performed in Charalambous et al.[9] suggest an oxygen vacancy buildup and the potential formation of reduced phases along the boundaries, causing depletion of holes and release of free electrons. As mentioned in Charalambous et al.,[7] the electric field in Charalambous et al.[9] and Dong and Chen[10] was turned off at furnace temperatures exceeding 1100°C, which potentially allowed modification of the microstructure by reoxidation, diffusion or other effects during furnace cool down.

In an investigation by Bechteler and Todd,[1] where the applied electric field was maintained during furnace cool down, the phenomenon of blackening in 3YSZ was associated with the electrochemically induced lattice modification and phase transformation from its usually tetragonal crystallographic structure to the FCC rocksalt ZrO structure with a lattice parameter of 0.458 nm, if electrochemically reduced in argon (Ar). If the same procedure is conducted in a nitrogen ($N_2$) containing atmosphere such as air or pure $N_2$, Zr(O,N) is formed,[1] as has also been reported by Morisaki et al.[11]

Recently, Sakamoto et al. observed the formation of 10- to 20-nm-sized ellipsoidal Zr(O,N) grains in cubic 8YSZ after electrical loading in air, which showed an alignment with the cubic 8YSZ structure.[12] Although it is clear from this previous work that electrochemical loading can cause a phase transformation in 8YSZ, the distribution of the new phase on the scale of several grains, the distribution of the yttrium dopant and other elements, and the crystallinity of the new phase during and after electrical loading of 8YSZ remain to be investigated. These may be modified if reoxidation of the material occurs during furnace cool down. The present work avoids the problem of reoxidation by maintaining an inert oxygen-free atmosphere during cooling and investigates the other aspects mentioned using SEM-EDS, XRD, and Raman spectroscopy. This also enables a comparison of the electrochemical reduction behavior between the mainly tetragonal 3YSZ reported previously and the mainly cubic 8YSZ in this work.

## 2 | MATERIALS AND METHODS

8YSZ ready to sinter powder (Tosoh, TZ-8YB) with a particle size of 150 nm was used. This was uniaxially pressed (200 MPa) into bar-shaped samples (30 × 5 × 3 $mm^3$), debinded in air at 600°C for 1 h, and pre-sintered in air up to >98% relative density at 1400°C for 1 h.

Two holes near the ends of the samples were manually drilled before sintering for attaching Pt-wires as electrodes. Pt paste was applied to reduce contact resistance between the wires and the sample.

Samples were placed in an alumina tube furnace, shown in greater detail in Bechteler et al.,[13] which was heated at 600°C/h to 800°C in oxygen ($O_2$). As soon as the furnace reached the defined temperature, the electric field was applied and increased stepwise to 30 V, which led to an increase in current and power dissipation. LabVIEW software was used to control the DC-power supply (EA-PSI 9750–60; EA Elektro-Automatik GmbH & Co. KG) and to record the electrical data. For experiments with a power limit of 20 W, the power supply changed to power control as soon as this limit was reached. In the case of higher power limits, the voltage was ramped up further to enable the limit to be reached. Power dissipation was maintained for 5 min before the atmosphere was changed to air and for another 5 min before the atmosphere was changed to argon (Ar) or nitrogen ($N_2$). Atmospheric changes were achieved by opening or closing the high-pressure gas cylinders connected on one side of the furnace, resulting in a continuous replacement of the original atmosphere, which exited the furnace on the opposite side. After the final atmospheric change, power dissipation was held for another 5 min before the furnace was turned off and furnace cool down started. The final atmosphere was maintained during cooling down and the electrical field was turned off when the furnace temperature dropped below 50°C.

When cooled, the electrically treated samples were transferred directly into an Ar-filled air-tight glove box to prevent reactions with the atmosphere such as reoxidation.

Mechanical grinding and polishing of the materials were performed with a Buehler grinding machine initially using diamond abrasives. The final polishing step was performed with colloidal silica. Thermal etching prior to some SEM investigations was conducted at 1150°C for 30 min in air using a heating rate of 600°C/h.

For the microstructural investigation before and after electrical loading, SEM (Merlin (FEG) SEM, Zeiss) images

were taken from sample surfaces. EDS (QUANTAX FlatQUAD, Bruker) was conducted to determine the elemental distribution in these regions. Samples were coated with 3 nm Pt prior to the investigation.

Grain size was measured on polished surfaces using the linear intercept method (>100 intercepts). No correction factor was applied.

XRD characterization of the samples was conducted in a rotating Ar-filled sample holder between $2\theta = 20°$ and 120° with a scan rate of 0.04°/s (Cu K$\alpha$ $\lambda = 1.5406$ Å, Empyrean, Malvern Panalytical GmbH). Furthermore, the region between 33° and 44° was characterized with a lower scan speed of 0.02°/s to improve the signal-to-noise ratio. Rietveld refinement of the XRD spectra was conducted within Profex software.[14] Cubic YSZ (space group 225, Fm-3 m), FCC rocksalt structured ZrO (space group 225, Fm-3 m), and pyrochlore $Y_2Zr_2O_7$ (space group 227, Fd-3 m) were considered for the refinement.

Raman microspectroscopy was performed on as-treated surfaces of bulk samples at room temperature using a Renishaw (UK) Raman 1000 System, equipped with a 632.8 nm 50 mW He-Ne laser.

## 3 | RESULTS

### 3.1 | Electrical loading procedure

Figure 1 shows the results for an 8YSZ sample electrically loaded in changing atmospheres starting with a stage in pure oxygen ($O_2$), described as stage I. The ramp of the electrical field up to 35 V (17.5 V/cm) at a furnace temperature of 800°C led to an increase in current and power dissipation up to the point where the initially defined power limit of 30 W led to a change to power-controlled stage II after ~400 s. The sample resistance reduced significantly during the transient stage (Figure 1B). The increase in power dissipation also led to a brighter sample appearance, from no electrical heating shown in Figure 1C up to the defined power dissipation limit in Figure 1E, due to emission of thermal radiation[15–17] owing to the increase in sample temperature by Joule heating.

Stage III is represented by an atmospheric change from $O_2$ to air, highlighted with a gray background in Figure 1A,B, starting after a total time of 700 s without changing the electrical parameters. Compared to stage II, a slight drop in resistance can be detected but no major changes can be seen in the electrical response.

Stages IV and V are defined by an increase in power dissipation from 30 to 35 W after 1000 s, and 40 W after 1300 s, respectively, whereby the electrical resistance of the sample decreased with increased power dissipation. Dependent on the power dissipation, the estimated sample surface temperature, assumed uniform,[18–20] reaches 1043°C for 20 W, 1197°C for 40 W, and 1314°C for 60 W power dissipation at a furnace temperature of 800°C.

After a total time of 1500 s, the atmosphere was changed from air to nitrogen ($N_2$) or argon (Ar), described as stage VI, highlighted with a blue background in Figure 1A,B. Following this atmospheric change, there was a slight increase in specimen resistance for approximately 10 s after which the sample resistance dropped quickly, plateauing at less than half its previous value in air after about 300 s, as shown in Figure 1B for Ar. During this time, the applied voltage dropped and the current increased significantly to maintain the 40 W power limit. The sample heating in this stage became even more inhomogeneous as shown in Figure 1F,G, which started on the cathode (left) side of the sample (Figure 1F) and shifted more toward the anode (right) side of the sample (Figure 1G).

Finally, following stage VI, the furnace was turned off after a total time of 2100 s. During furnace cool down, power dissipation was still maintained in Ar or $N_2$ to the point where the furnace temperature dropped below 50°C, which took approximately 2 h, whereupon the power supply was turned off. The electrically heated sample, just before turning off the power supply, is shown in Figure 1H and shows a comparable localized heating to the sample at an environmental temperature of 800°C (Figure 1G).

The electrical resistance at a power dissipation of 40 W in Ar during furnace cool down decreased from ≈6 Ω at 800°C furnace temperature, estimated sample temperature of 1197°C, to ≈3 Ω at 50°C furnace temperature, estimated sample temperature of 1080°C, between the point where the furnace was turned off and when the sample was taken from the furnace, indicating that the electrical resistance of the sample decreased with decreasing sample temperature (PTC behavior). The sample showed some cracking on the surface, which sometimes even led to through-thickness cracking of the sample during such electrical loading processes.

The sample taken from the furnace after electrical loading in Ar, as shown in Figure 1I,J, shows a metallic golden brown and black coloring with some finger-shaped regions, as reported by others for electrochemically reduced YSZ.[1–3,11,12]

The electrical results, as well as the sample appearance, for electrical loading during an atmospheric change from air to nitrogen ($N_2$) at 60 W power dissipation, including sample appearance post-treatment, are shown with expanded time scales in Figures S1 and S2. The main difference in $N_2$ compared with Ar is a more golden color.

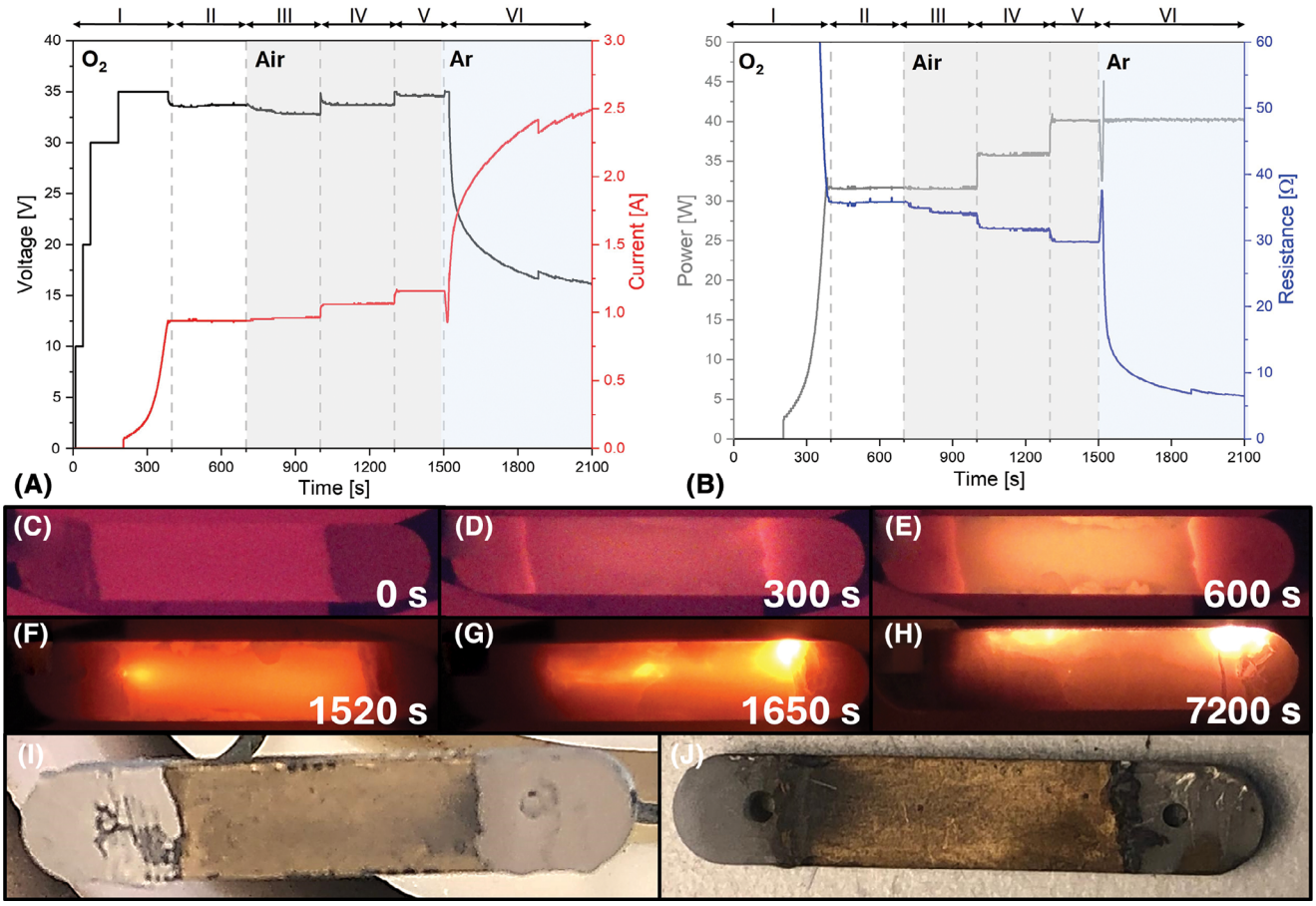


**FIGURE 1** Electrical loading procedure on 8YSZ (8 mol% yttria-stabilized zirconia) in changing atmosphere, starting in oxygen ($O_2$), and transitioning into air and argon (Ar) with the cathode being located on the left and the anode on the right; (A and B) the electrical parameters including applied voltage and current in (A), and calculated power and resistance in (B); (C to H) the sample at various points throughout the loading procedure; (I and J) the sample after electrical loading, whereby (I) shows the sample surface facing the camera and J) the opposite side facing away from the camera.

## 3.2 | Microstructure

### 3.2.1 | Surface

All of the following SEM images are taken from an 8YSZ sample electrically loaded with Ar as the final atmosphere and with a maximum power dissipation of 40 W. Samples electrically loaded in $N_2$ exhibited similar morphologies and structures without significant deviations, and some of them are shown in the Supporting Information.

Figure 2 shows the surface of an 8YSZ sample, which at lower magnification (Figure 2A) still shows the grain size and shape of the conventionally sintered material (grain size 1.8 ± 0.2 µm). At higher magnifications (Figure 2B–F), the surface consists of many small crystals approximately 100 nm in size. Furthermore, there are several macro- (Figure 2A) and micro-cracks (Figure 2C,D) along grain boundaries and through several grains. A few pores, as can be observed in conventionally sintered 8YSZ without electrical loading (Figure S3), can be seen at triple points, as shown in Figure 2A. However, there are no submicron pores along the grain boundaries.

If the surface of electrically loaded 8YSZ was lightly polished to remove the surface relief (1 µm diamond and colloidal silica), the ~100 nm crystals mentioned above could be seen as bright regions within a darker matrix, as shown in Figure 3.

In Figure 4, a SEM image and EDS elemental distribution maps of the electrically loaded and lightly polished sample surface show the 100 nm structures within the matrix material. As shown in Figure 3, in some grains, the concentration of the 100 nm structures is significantly higher than it is in others, which could be caused by an inhomogeneous reduction of some areas or grains. The oxygen (O) distribution in Figure 4B shows that these submicron regions contain significantly lower oxygen and yttrium (Y) concentrations than the matrix, whereas the signal of zirconium (Zr) is increased.

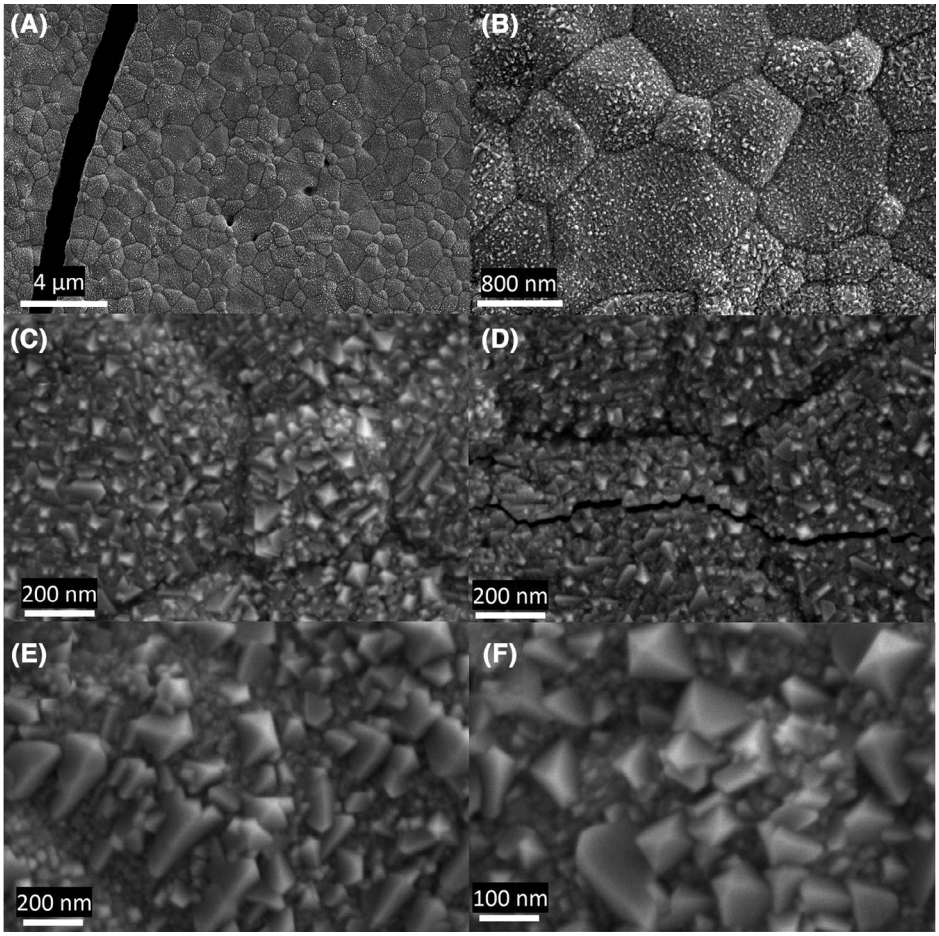


**FIGURE 2** SEM image of the surface of an 8YSZ sample after electrical loading in Ar with a power of 40 W at various positions and magnifications.

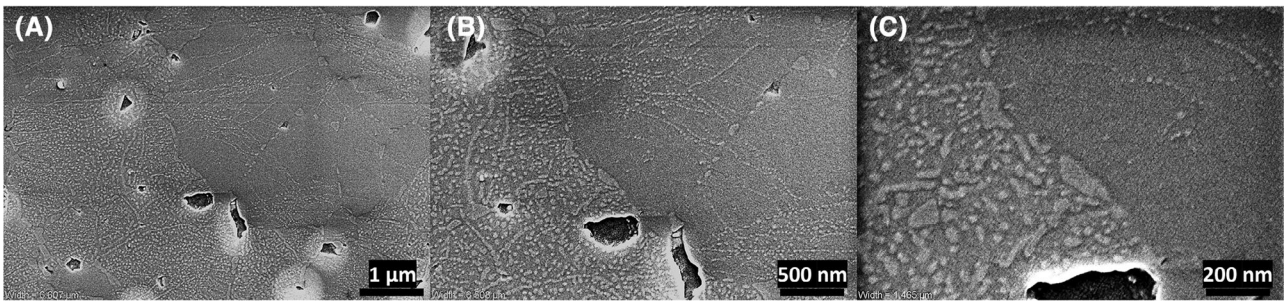


**FIGURE 3** SEM image of the gently polished surface of an 8YSZ sample after electrical loading in Ar with a power dissipation of 40 W at various magnifications.

EDS spectra taken from four different points, highlighted in the SEM image in Figure 4A, are shown in Figure 4E. The spectra are normalized to 1 for the Zr L$\alpha$ signal around an energy of 2.04 keV to identify the relative change in O and Y concentration between a matrix region (8YSZ, black) and three submicron regions (ZrO-1, red; ZrO-2, green; ZrO-3, blue). The detailed O region of the spectra shown in Figure 4F shows that compared to the matrix region (8YSZ, black), which shows a normalized O signal of 0.87, the submicron regions are significantly lower in O concentration, down to 0.56 normalized intensity for ZrO-2 (green). The Y signal is also diminished in the submicron regions shown in Figure 4G, though some Y remains. A background-subtracted and isolated Y signal is shown in Figure S4.

SEM images and EDS maps of the polished surface and the fractured cross-section of an 8YSZ sample loaded in $N_2$ are shown in Figures S5 and S6.

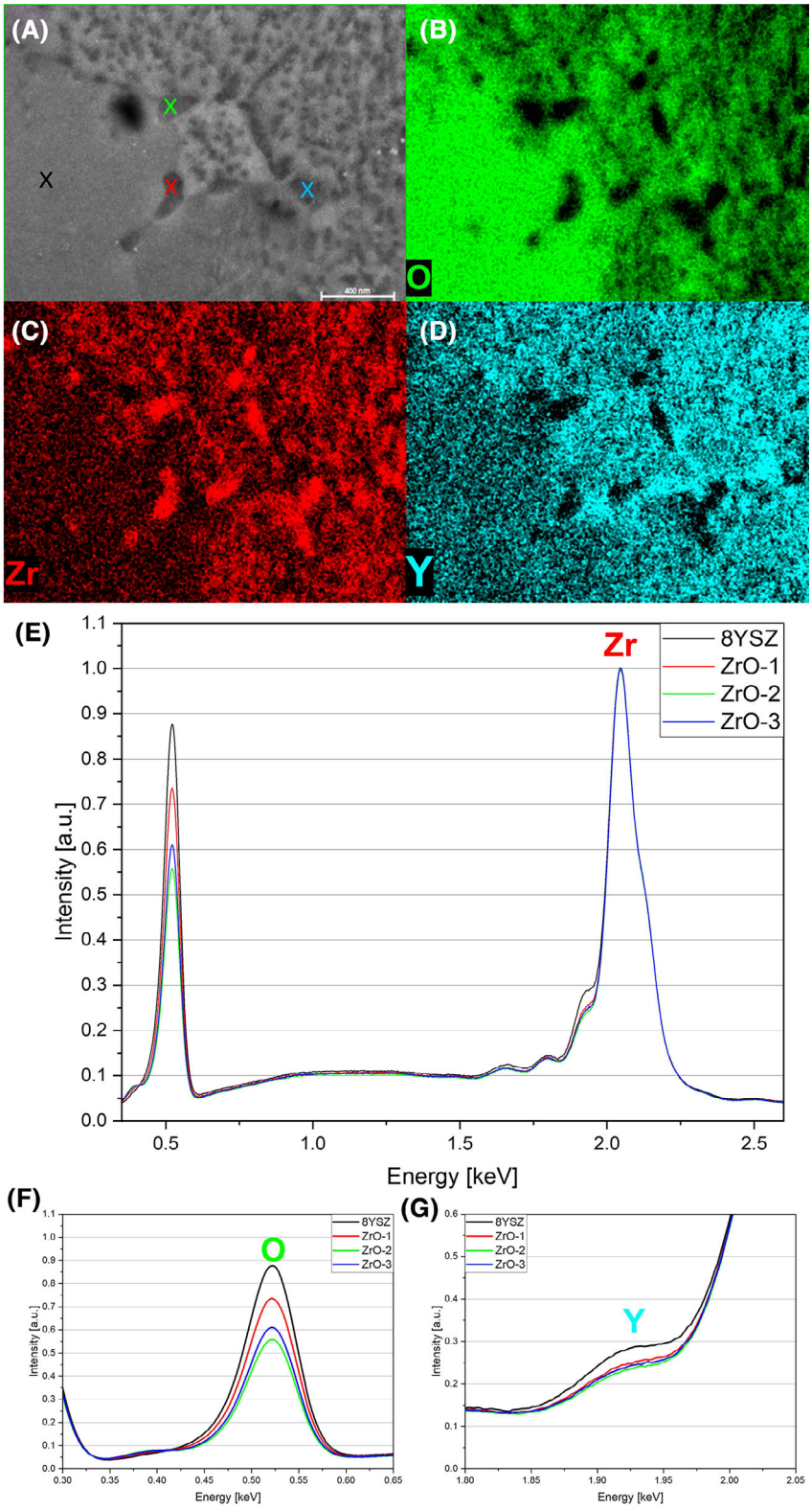


**FIGURE 4** SEM image (A) and elemental distribution maps showing (B) oxygen in green, (C) zirconium in red, and (D) yttrium in blue; (E) four EDS spectra taken from several points highlighted in (A) with the corresponding color with the spectra being normalized to 1 at the Zr signal; (F) the section of the EDS spectra where the signal for oxygen is located; (G) the EDS spectra region where yttrium is located. All images and spectra are taken from an 8YSZ sample electrically loaded at 40 W in Ar.

### 3.2.2 | Cross-section

*Fractured cross-section*

Figure 5A–I shows the central region of the fractured cross-section of an electrically loaded 8YSZ sample at 40 W in Ar at different magnifications. SEM images of the near-surface fractured cross-section of an electrically loaded 8YSZ sample are shown in Figure 5J–M, which resemble the appearance of the central cross-section. The average grain size is 1.7 ± 0.3 μm, which is very similar to that of the conventionally sintered 8YSZ sample without electrical loading (1.8 ± 0.2 μm). Clear

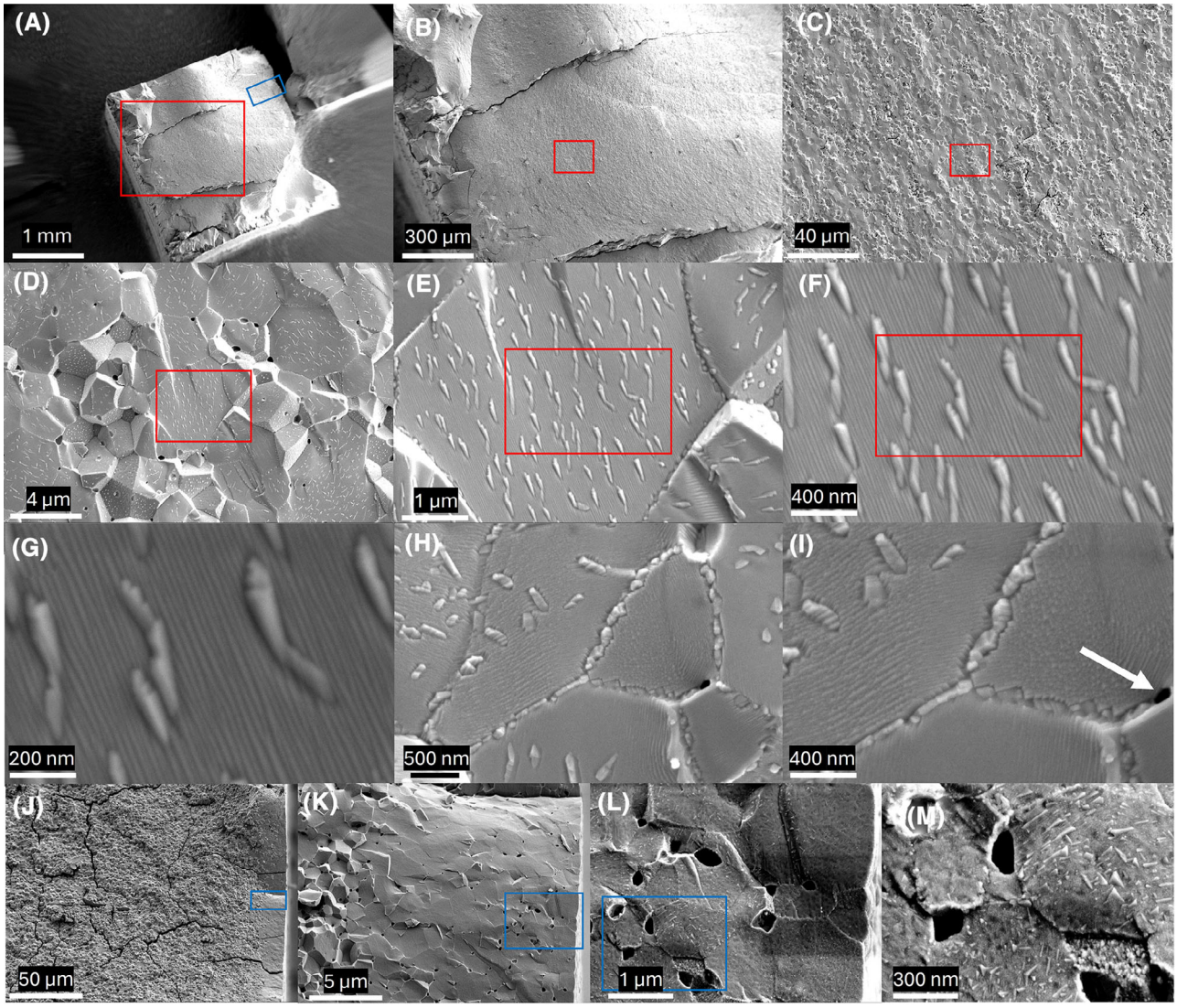


**FIGURE 5** Fractured cross-section of an electrically loaded 8YSZ sample at low magnification (A) and other higher magnifications and regions. The red boxes indicate the area of the sample shown in the following SEM image at higher magnification in the central cross-section of the sample from image (B) to (I). Images (H) and (I) show a central cross-section of the sample with a focus region around grain boundaries showing precipitations. Regions shown and highlighted in blue boxes, from (J) to (M), are located on the near surface cross-section.

signs of cracking can be seen throughout the sample in the SEM images. Furthermore, the fracture was mainly transgranular, with some randomly located regions of intergranular fracture, which vary in size and account for only ≈20% of the cross-section. This contrasts with the 8YSZ sample without electrical loading, as shown in Figure S3, in which fracture was almost completely intergranular.

Figure 5B–I shows the central cross-sections at higher magnifications to show the precipitates more clearly, which can also be seen close to the surface as shown in Figure 5M. The precipitates tend to be aligned with the striations evident on the fractured matrix surrounding them. The alignment is not perfect, however, suggesting that the precipitates lose their relationship with the matrix as they grow.

Within submicron grains, fewer such structures can be found, as shown in Figure 5H. Compared to the inside of the grains, where these structures are more or less evenly distributed, a higher concentration of such precipitates can be found along the grain boundaries, which are almost fully covered as shown in Figure 5H,I. As well as the rather big pores located on the triple points shown in Figure 5L,M, a few small pores can be detected on the grain boundaries, which show similar shape and size to the precipitates. One of the larger of these is highlighted with a white arrow in Figure 5I, and Figure S7 shows smaller pores around and between the grain boundary precipitates.

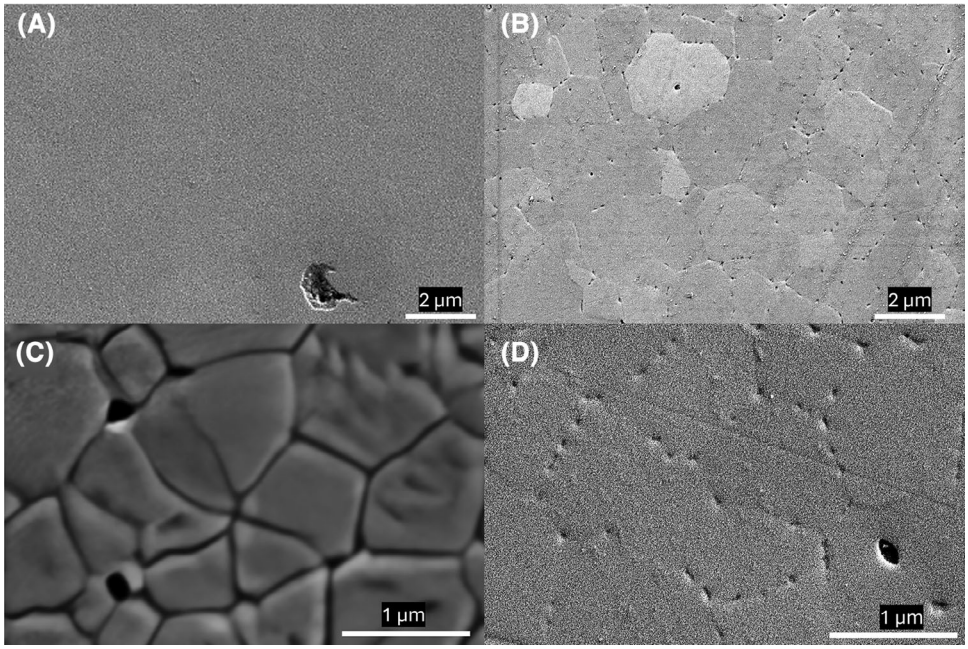


**FIGURE 6** SEM images of the polished unetched (A) and etched (C) cross-section of conventionally sintered 8YSZ without electrical loading; (B and D) SEM images of the polished cross-section of an electrically loaded 8YSZ.

The structuring of the matrix fracture surfaces surrounding the small precipitates, exhibited most clearly in Figure 5F,G, was not seen in the few grains with transgranular fracture in as-conventionally sintered 8YSZ. Because of that, it can be assumed that this phenomenon is also related to the electrical loading process.

*Polished cross-section*

Figure 6A,C shows SEM images taken from polished unetched (A) and etched (C) cross-sections of a conventionally sintered 8YSZ sample with no electrical loading. One pore can be seen at the bottom of Figure 6A with no other unusual features and a similar contrast throughout the image. Figure 6C shows some small pores at the triple points, however no pores are visible along grain boundaries.

A polished unetched cross-section of an electrically loaded 8YSZ sample at 40 W in Ar is shown in Figure 6B,D at different magnifications, where submicron pores can be observed along almost every grain boundary, and a few submicron pores can also be found within some of the grains. Furthermore, in a few grains the grain interiors themselves show a different contrast to each other, which was not observed in the unloaded sample (Figure 6A). This could potentially point toward a change in the interior of some of the grains due to the electrical loading procedure, which might be caused by the extraction of oxygen from the grains and a changing ratio of cations and anions. As remarked in connection with Figure 5, small pores can also be seen on the grain boundaries.

## 3.3 | Phase structure

### 3.3.1 | XRD

Figure 7A–C shows the background corrected XRD spectra obtained from a conventionally sintered 8YSZ sample (Conv., black) with a refined lattice parameter of 0.514 nm. Only one phase (FCC fluorite) was needed for the refinement, which is shown in Figure S8.

The samples electrically loaded in $N_2$ show a loss of clear separation of the {200} $K_{\alpha1}$ and $K_{\alpha2}$ peaks located around 35° indicating peak broadening, though there was little change in peak position. Furthermore, new peaks, mostly identified as the rocksalt structure Zr(O,N) phase, were present after electrical loading. Results containing refined phase contents and lattice parameters are summarized in Table 1.

The general trend of the samples investigated showed that the lattice parameter for the FCC fluorite phase remained constant at 0.514 nm for all atmospheres and power dissipations. With an increase in power dissipation in $N_2$, the proportion of Zr(O,N) increased from 8 to 51 wt.%, mainly at the expense of the fluorite matrix. At a power dissipation of 60 W, an additional diffraction peak at 29.50°, shown with higher resolution in Figure S9, emerged, which could most likely be associated with the formation of pyrochlore $Y_2Zr_2O_7$ and its most intense peak {222}.[21–23] According to the refinement, a concentration of 5 wt.% and a lattice parameter of 1.049 nm were estimated from this single peak, which is comparable to other

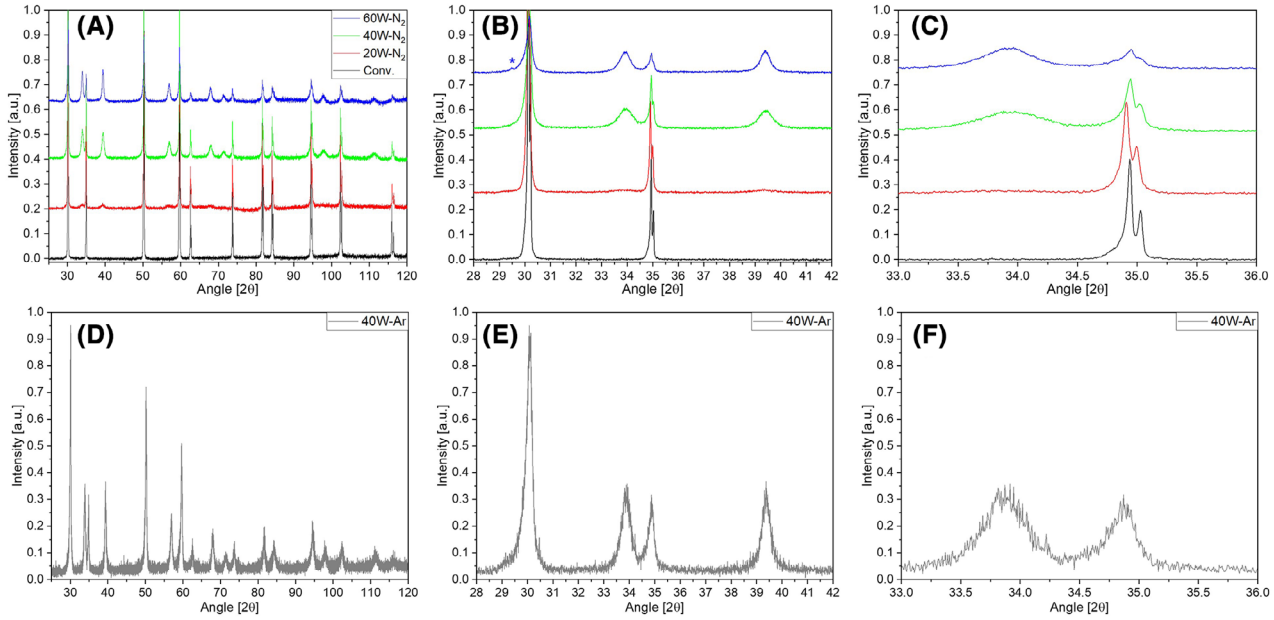


**FIGURE 7** X-ray diffraction (XRD) spectra of conventionally sintered (Conv.) and electrically loaded 8YSZ; (A) the XRD scan between 25° and 120° for conventionally sintered and in $N_2$-loaded 8YSZ with a power dissipation of 20, 40, or 60 W; (B) the detailed scan between 28° and 42°, with an even higher grade of detail shown in (C) from 33° to 36°; (D) the XRD scan between 25° and 120° for in Ar-loaded 8YSZ with a power dissipation of 40 W, with more detail of selected regions shown in (E) and (F).

**TABLE 1** Rietveld refinement results for the X-ray diffraction (XRD) scans shown in Figure 8 including refined lattice parameters (a) and ratios of phase content in wt.% for FCC fluorite 8YSZ (8 mol% yttria-stabilized zirconia), FCC rocksalt Zr(O,N), and pyrochlore zirconate ($Y_2Zr_2O_7$).

| | FCC fluorite YSZ | | FCC rocksalt Zr(O,N) | | $Y_2Zr_2O_7$ | |
|---|---|---|---|---|---|---|
| **Sample** | ***a* (nm)** | **Ratio (wt.%)** | ***a* (nm)** | **Ratio (wt.%)** | ***a* (nm)** | **Ratio (wt.%)** |
| **Conventional** | 0.514 | 100 | – | – | – | – |
| **20W-$N_2$** | 0.514 | 92 | 0.458 | 8 | – | – |
| **40W-$N_2$** | 0.514 | 56 | 0.458 | 44 | – | – |
| **60W-$N_2$** | 0.514 | 44 | 0.458 | 51 | 1.049 | 5 |
| **40W-Ar** | 0.514 | 53 | 0.457 | 47 | – | – |

theoretically and experimentally suggested lattice parameters for this phase, ranging from 1.034[24] to 1.0474 nm.[21]

If the conventionally sintered 8YSZ sample was loaded with 40 W in Ar, a content of 53 wt.% of FCC fluorite YSZ was calculated, again with a lattice parameter of 0.514 nm. However, the {200} K$\alpha_1$ and K$\alpha_2$ peaks around 35° merged to one single peak at 34.88° (Figure 7D–F), indicating considerable peak broadening. Since no nitrogen was available to form Zr(O,N), the rocksalt structure identified is described as ZrO, with a lattice parameter of 0.457 nm and a content of 47 wt.%.

### 3.3.2 | Raman spectroscopy

Conventionally sintered 8YSZ shows the expected Raman spectrum for fluorite structure $ZrO_2$[25] with a relatively strong signal between the two diffuse "peaks" located at 150 $cm^{-1}$ and 622 $cm^{-1}$, as shown in Figure 8A. Otherwise, no distinct peaks were detected for this sample.

If the material was electrically loaded in $N_2$, the Raman spectrum became more intense as the power limit increased, and distinct peaks at 167 $cm^{-1}$ and 224 $cm^{-1}$ developed as shown in Figure 8A, along with a broad peak at around 500 $cm^{-1}$ with several shoulders. Another less intense peak emerged at 984 $cm^{-1}$. Similar peaks were detected in the cross-section of the sample.

A comparable Raman spectrum was obtained from an 8YSZ sample loaded with 40 W in Ar, as shown in Figure 8B. However, the peaks at 167 and 220 $cm^{-1}$ are less clear compared to the samples loaded in $N_2$. Furthermore, the shoulders of the broad 500 $cm^{-1}$ peak of the $N_2$ samples became resolved into clearer peaks at Raman shifts of 331, 394, 485, 583, and 975 $cm^{-1}$ after loading in Ar.

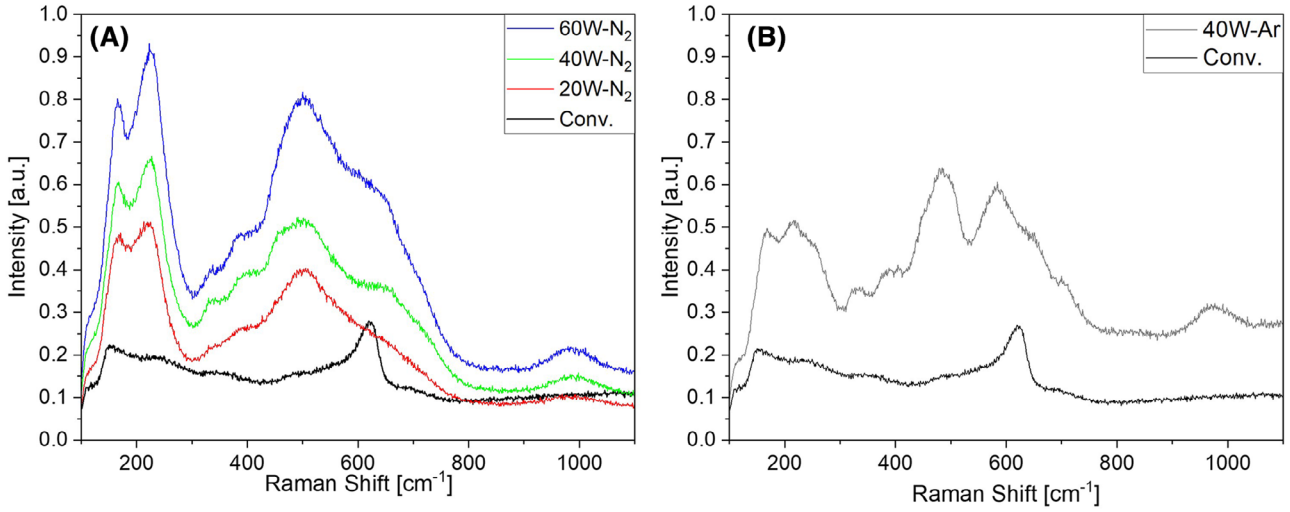


**FIGURE 8** Raman spectra of conventionally sintered (Conv.) and electrically loaded 8YSZ in (A) $N_2$ with a power dissipation of 20, 40, or 60 W; (B) Ar with a power dissipation of 40 W.

## 4 | DISCUSSION

### 4.1 | Electrical loading response

The application of an electric field of 35 V (17.5 V/cm) in $O_2$ caused a rapid increase in current and power dissipation up to a defined power limit of 30 W, which led to a transition from voltage to power control and a transition from stage I to stage II. In stage II, the sample heating and emission of thermal radiation[15–17] is rather homogeneous, with localized heating at the Pt-paste/8YSZ interface.

After changing atmospheres from $O_2$ to air, marking the beginning of stage III, the resistance of the material slightly decreased, which can most likely be associated with an ongoing electrochemical reduction of the material and an increase in conductivity by such a process, since the power dissipation and estimated sample temperature did not change. This assumption is supported by the comparatively long time (>50 s) that it takes for the resistance to decrease and the fact that densification and a significant change in power dissipation/sample temperature can be ruled out. Further increase in power dissipation in stages IV and V in air leads to an increase in estimated sample temperature and drop in resistance, which is commonly attributed to the corresponding increase in sample temperature.

An atmospheric change from air to argon (Ar) (Figure 1) or nitrogen ($N_2$, Figures S1 and S2), thereby reducing the oxygen partial pressure, led initially to an increase in specimen resistance but after a short time, the resistance decreased rapidly as observed in previous investigations.[6,7,12] This behavior can be explained by an initial decrease in ionic conduction owing to the lack of oxygen immediately after the atmospheric change, which quickly transitioned into a stage where the electrochemical reduction, confirmed by the microstructural and crystallographic results, led to an increase in electronic conduction, first by extraction of oxygen from the fluorite lattice, and then by formation of the electronically conducting rocksalt phase.[7,26–28]

### 4.2 | Inhomogeneity of electrochemical reduction

The macroscopic localization of heating toward the anode and the centere of the cross-section is well known and originates, respectively, in the electrochemical reduction near the cathode lowering the resistivity, and heat loss at the specimen surface concentrating the current in the hotter interior, the latter also being exacerbated by the decreased resistivity along the electrochemically reduced current path. The inhomogeneity of the particle content and fracture mode suggests that the electrochemical reduction during electrical loading was also inhomogeneous on a mesoscopic length scale, several grains in dimensions. Janek and Korte[3] showed that the higher conductivity of electrochemically reduced YSZ leads to instability at high electric fields, causing the dendritic growth of fingers of reduced material from the cathode. Percolative conductive pathways in green bodies have also been predicted numerically owing to electrochemical and interfacial effects.[29] Although our materials were pre-sintered, the effects of grain boundaries, triple points, and different grain orientations can still be expected to encourage such percolative pathways. It is therefore suggested that the increased electronic conductivity of reduced 8YSZ coupled with microstructural effects is responsible for the

non-uniform electrochemical reduction observed in this work.

## 4.3 | Fracture behavior and pore formation

Prior to electrical loading, the fracture mode of the 8YSZ was almost completely intergranular (Figure S3) but the fracture mode of the electrically loaded ceramic was about 80% transgranular (Figure 5) with regions of intergranular fracture. This inhomogeneity in fracture mode may be associated with the non-uniform distribution of the Zr(O,N) nanoparticles shown in various figures in this work, as almost all regions with transgranular fracture showed the presence of these particles and few particles could be seen on the grain boundaries in regions of intergranular fracture.

One reason for the change in fracture mode in the heavily reduced regions may be that the intergranular Zr(O,N) particles perturb the propagation of cracks traveling along the grain boundaries, causing deflection into the grains. This is a common observation in ceramic nanocomposites and may occur if the particles are tougher or stiffer than the fluorite matrix, are well bonded to the grains, or are under compressive thermal residual stress.[30–32] Zr(O,N) and ZrN have higher stiffness and lower thermal expansion coefficient than cubic 8YSZ,[33,34] so the stiffness and thermal residual stress criteria support this explanation.

The bonding of the particles to the matrix is more difficult to assess but the fracture surfaces do not show holes indicating extensive pullout of particles from one half of the fracture surface, suggesting that the particles were sufficiently well bonded for the cracks to pass through most of them. This is also consistent with the involvement of the particles in the change of fracture mode.

When the cross-section was mechanically polished the microstructure showed some grain boundary porosity (Figure 6) and although limited particle pullout during polishing or preferential erosion of the rocksalt precipitates cannot be ruled out, some of the pores in the polished surface presumably correspond to the gaps between and around the particles shown in the fracture surface (Figure 5 and Figure S7). It has been suggested[1,12] that the FCC cation sublattice initially remains in place during transformation from fluorite to rocksalt, and a simple explanation for the pores associated with the particles is provided by the large volumetric change of −29% for the unit cell calculated from the lattice parameters in Table 1. In other investigations, submicron pores along the grain boundaries have been associated with the direct condensation of oxygen vacancies[9,10] but the present observations suggest an additional mechanism involving the formation of the rocksalt phase.

The macro- and micro-cracking observed has also been observed by other studies[7,10] and can be related to residual stresses caused by the change in crystallographic structure, lattice parameter, and volume during formation of the rocksalt phase. Given the large volumetric change and inhomogeneity of the phase transformation, it is easy to see how very large internal stresses may result to add to the thermal stress caused by the non-uniform heating of the sample shown in Figure 1 and Figure S1.

The SEM images of transgranular fracture surfaces in Figure 5 show striations within the fluorite grains, which were not present in the previously published STEM images[12] or in the few transgranular fractures in the as-sintered 8YSZ (Figure S3). Sakamoto et al. who found that the Zr(O,N) particles nucleate as crystals of 10–20 nm in size, aligned with their {001} planes parallel to those of the original 8YSZ grains[12] so the alignment of the striations with the particles in this work suggests that they are crystallographic in origin. The broadening of the XRD peaks (Figure 7) shows that the originally highly crystalline fluorite structure of 8YSZ became more defective during electrical loading. This could be attributed to the formation of oxygen vacancies by electrochemical reduction and the segregation of the Y dopant from the Zr(O,N) shown by the EDS results in Figure 4 and Figures S5 and S6. Flash sintering has also been shown to increase the density of dislocations and other lattice defects.[35,36] The striations could be related to the limited ordering of the excess oxygen vacancies or the Y rejected from the Zr(O,N). The defective nature of the grains may reduce their toughness, which would also favor transgranular fracture. However, the reason for this structuring of the fracture surfaces remains to be confirmed and requires further investigation.

## 4.4 | Formation and structure of rocksalt Zr(O,N) in YSZ

The generation of a rocksalt phase during DC FS of cubic 8YSZ in air noted by Charalambous et al.[7] and Sakamoto et al.[12] was confirmed by the XRD and Raman results in this investigation. The presence of N was demonstrated by EELS in Sakamoto et al.[12] and since the experiments of Charalambous et al.[7] were also conducted in air, it seems likely that Zr(O,N) rather than ZrO was the phase present in their work. Nevertheless, the present work strongly suggests that the formation of ZrO is also possible after electrical loading if $N_2$ is excluded by loading in Ar and follows a comparable behavior as for Zr(O,N).[7,9,12]

As for Zr(O,N) formed in tetragonal 3YSZ,[1] a rocksalt structure with a refined lattice parameter of 0.458 nm for

Zr(O,N) in 8YSZ loaded in nitrogen ($N_2$), and 0.457 nm for ZrO in 8YSZ loaded in Ar was formed. The similarity in unit cell sizes is because the Zr atom is large compared to O or N and defines the overall unit cell size.[1] These results show that the extraction of oxygen by electrical loading in an inert atmosphere leads to the formation of the same rocksalt ZrO or Zr(O,N), depending on the atmosphere applied, independent of the original zirconia phase or power dissipation.

There are also some differences, however. In the present work, it is evident that Y was rejected from the Zr(O,N) into the matrix. This was not observed in the case of 3YSZ. The implication is that the limit of solubility of Y in the ZrO loaded in Ar and Zr(O,N) loaded in $N_2$ atmosphere is between a cation content of 6 mol% (in 3YSZ) and 16 mol% (in 8YSZ). Using the EDS spectra in Figure 4, the Y concentration of the rocksalt phase can be estimated as ~50% of the conventionally sintered fluorite structure sample (shown in Figure S4), giving a solubility limit of Y cations in the Zr(O,N) phase of about 8 mol%, which agrees with the above estimate. The ejection of Y from the Zr(O,N) regions to the surrounding grains is the likely explanation for the formation of small amounts of $Y_2Zr_2O_7$.

The Raman spectra obtained from the Zr(O,N)-containing samples are comparable to Raman spectra obtained from Zr(O,N) films reported by other researchers,[37] adding further support to the phase identification. Since a defect-free FCC rocksalt structure should not show any Raman signal,[7,37–41] these results indicate that the ZrO and Zr(O,N) are highly defective.

The segregation of Y due to the formation of Zr(O,N) is interesting in the perspective of energy applications such as solid oxide fuel and electrolyzer cells (SOFCs, SOECs), where 8YSZ is often used as a solid electrolyte, because an electric field is applied for a long time at elevated temperatures in such applications[42–44] and the formation of the rocksalt phase and the segregation of stabilizers could lead to a change of the material's electrical behavior and microstructure. Although the voltages in fuel cells (~0.1–1 V) are much lower than those applied here, the zirconia electrolytes used are very thin (~10 μm). The corresponding mean electric fields of 100–1000 V/cm significantly exceed the maximum electric field applied in this work of 20 V/cm and also the minimum electric field to cause blackening of approximately 2 V/cm reported by Janek and Korte.[3] Although the electrode reactions and operating conditions in SOFCs and SOECs are different from ours, an ongoing electrochemical reduction during operation and reoxidation of the reduced material during interruptions where no field and current were applied would be consistent with, for example, the increase in cell voltage and resistance after such interruptions reported in Fang et al.[42] This effect is probably less important during FS because of the rather short process times and the potential reoxidation, diffusion, and restructuring during furnace cool down, where usually no electric field is applied.

Another apparent difference between the 8YSZ investigated here and 3YSZ investigated in Bechteler and Todd[1] is that in the present case, many of the rocksalt particles are at grain boundaries and on the surface of the sample. This was not the case in tetragonal 3YSZ, where whole grains transformed into the rocksalt phase.[1] This could be related to differences in the stability of the original phase or grain boundary structure and composition segregation, but could also relate to the grain size of the matrix phase, which is approximately five times the size in the present case compared with the tetragonal 3YSZ grains shown in Bechteler and Todd.[1] The smaller grain size of the 3YSZ would tend to mask the difference between the particles and the grains and to spread the rocksalt phase formed more sparingly over the greater area of grain boundary.

The solubility of other common dopants for zirconia, such as magnesium (Mg), in Zr(O,N) remains to be investigated and is the subject of a follow-up study.

## 5 | CONCLUSIONS

1. Originally fluorite structure 8YSZ formed defective rocksalt structure ZrO or Zr(O,N) with lattice parameters of 0.457 and 0.458 nm during DC electrical loading in an Ar or $N_2$ atmosphere, respectively.
2. In cubic 8YSZ, the Zr(O,N) phase formed precipitates approximately 100 nm in size. Some of these were located within the grains but mainly formed along grain boundaries and surfaces, in contrast to the case in 3YSZ.
3. The reduction and particle formation were inhomogeneous on all length scales between the grain size and the dimensions of the sample.
4. The reduction and rocksalt particle formation caused a change in fracture mode from intergranular in unreduced material to transgranular.
5. The large volume reduction on the formation of the ZrO or Zr(O,N) was associated with pore formation and cracking.
6. Compared to tetragonal 3YSZ, the cubic 8YSZ material showed strong segregation of the Y dopant from the Zr(O,N) precipitates into the matrix.

## ACKNOWLEDGMENTS

This work was supported by the Engineering and Physical Sciences Research Council (EP/T517811/1) and the Studienstiftung des deutschen Volkes—German Academic Scholarship Foundation.

The authors acknowledge use of characterization facilities within the David Cockayne Centre for Electron

Microscopy, Department of Materials, University of Oxford, alongside financial support provided by the Henry Royce Institute (Grant No. EP/R010145/1).

## ORCID

*Christian Bechteler* https://orcid.org/0000-0003-0706-9863

*Richard I. Todd* https://orcid.org/0000-0002-6990-5794

## REFERENCES

1. Bechteler C, Todd RI. Lattice modification of $ZrO_2$-$\delta$ and formation of rocksalt structure ZrO and Zr(O,N) after DC electrical loading of 3YSZ. J Eur Ceram Soc. 2024;44:1044–52. https://doi.org/10.1016/J.JEURCERAMSOC.2023.09.014
2. Biesuz M, Pinter L, Saunders T, Reece M, Binner J, Sglavo VM, et al. Investigation of electrochemical, optical and thermal effects during flash sintering of 8YSZ. Materials. 2018;11(7):1214. https://doi.org/10.3390/MA11071214
3. Janek J, Korte C. Electrochemical blackening of yttria-stabilized zirconia—Morphological instability of the moving reaction front. Solid State Ion. 1999;116(3–4):181–95. https://doi.org/10.1016/S0167-2738(98)00415-9
4. Farley JM, Thorp JS, Ross JS, Saunders GA. Effect of current-blackening on the elastic constants of yttria-stabilised zirconia. J Mater Sci. 1972;7(4):475–76. https://doi.org/10.1007/BF02403413
5. Wright DA, Thorp JS, Aypar A, Buckley HP. Optical absorption in current-blackened yttria-stabilized zirconia. J Mater Sci. 1973;8(6):876–82. https://doi.org/10.1007/BF02397918/METRICS
6. Alvarez A, Dong Y, Chen IW. DC electrical degradation of YSZ: voltage-controlled electrical metallization of a fast ion conducting insulator. J Am Ceram Soc. 2020;103(5):3178–93. https://doi.org/10.1111/JACE.17004
7. Charalambous H, Jha SK, Okasinski JS, Tsakalakos T. Generation of electric-field stabilized zirconium monoxide secondary phase within cubic zirconia. Scr Mater. 2021;190:22–26. https://doi.org/10.1016/J.SCRIPTAMAT.2020.08.026
8. Schönberg N, Heimbürger G, Matikkala EJ, Sörensen NA. The structure of the metallic quaternary phase ZrTaNO. Acta Chem Scand. 1954;8:627–29. https://doi.org/10.3891/ACTA.CHEM.SCAND.08-0627
9. Charalambous H, Jha SK, Vikrant KSN, Garcıá RE, Phuah XL, Wang H, et al. Electric field-induced grain boundary degradation mechanism in yttria stabilized zirconia. Scr Mater. 2021;204:114130. https://doi.org/10.1016/j.scriptamat.2021.114130
10. Dong Y, Chen I. Electrical and hydrogen reduction enhances kinetics in doped zirconia and ceria: II . Mapping electrode polarization and vacancy condensation in YSZ. J Am Ceram Soc. 2018;101(3):1058–73. https://doi.org/10.1111/jace.15274
11. Morisaki N, Yoshida H, Matsui K, Tokunaga T, Sasaki K, Yamamoto T. Synthesis of zirconium oxynitride in air under DC electric fields. Appl Phys Lett. 2016;109(8):083104. https://doi.org/10.1063/1.4961624
12. Sakamoto S, Kodaira A, Tokunaga T, Morisaki N, Kobayashi K, Yamamoto T. Microstructure analysis for zirconium oxynitrides formed in 8 mol% yttria-doped zirconia by a flash event under a direct current electric field in an ambient atmosphere. J Eur Ceram Soc. 2025;45:117265. https://doi.org/10.1016/j.jeurceramsoc.2025.117265
13. Bechteler C, Gibson A, Falco S, Kirkpatrick A, Todd RI. Plasma formation during flash sintering of boron carbide—part I: plasma characteristics. Ceram Int. 2024;50:37241–50. https://doi.org/10.1016/j.ceramint.2024.05.250
14. Doebelin N, Kleeberg R. Profex: a graphical user interface for the Rietveld refinement program BGMN. J Appl Crystallogr. 2015;48(5):1573–80. https://doi.org/10.1107/S1600576715014685
15. Bechteler C, Kirkpatrick A, Todd RI. Visible light emissions during flash sintering of 3YSZ are thermal radiation. Scr Mater.2022;219:114849. https://doi.org/10.1016/j.scriptamat.2022.114849
16. Bechteler C, Kirkpatrick A, Todd RI. Comment on 'flash in argon atmosphere yields electronically conducting yttria-stabilized zirconia at ambient temperature' by Jo et al., J Am Ceram Soc. 2023;106:5133–5139. J Am Ceram Soc. 2024;107:2776–77. https://doi.org/10.1111/jace.19593
17. Biesuz M, Luchi P, Quaranta A, Martucci A, Sglavo VM. Photoemission during flash sintering: an interpretation based on thermal radiation. J Eur Ceram Soc. 2017;37(9):3125–30. https://doi.org/10.1016/J.JEURCERAMSOC.2017.03.050
18. Raj R. Joule heating during flash-sintering. J Eur Ceram Soc. 2012;32(10):2293–301. https://doi.org/10.1016/j.jeurceramsoc.2012.02.030
19. Yoshida M, Falco S, Todd RI. Measurement and modelling of electrical resistivity by four-terminal method during flash sintering of 3YSZ. J Ceram Soc Jpn. 2018;126(7):579–90. https://doi.org/10.2109/jcersj2.17256
20. Todd RI, Zapata-Solvas E, Bonilla RS, Sneddon T, Wilshaw PR. Electrical characteristics of flash sintering: thermal runaway of joule heating. J Eur Ceram Soc. 2015;35(6):1865–77. https://doi.org/10.1016/j.jeurceramsoc.2014.12.022
21. Kumar M, Raj IA, Pattabiraman R. $Y2Zr_2O_7$ (YZ)-pyrochlore based oxide as an electrolyte material for intermediate temperature solid oxide fuel cells (ITSOFCs)-influence of Mn addition on YZ. Mater Chem Phys. 2008;108(1):102–8. https://doi.org/10.1016/j.matchemphys.2007.09.010
22. Tong Y, Xue P, Jian F, Lu L, Wang X, Yang X. Preparation and characterization of Y2Zr2O7 nanocrystals and their photocatalytic properties. Mater Sci Eng B. 2008;150(3):194–98. https://doi.org/10.1016/j.mseb.2008.04.009
23. Majumdar D, Chatterjee D. X-ray photoelectron spectroscopic studies on yttria, zirconia, and yttria-stabilized zirconia. J Appl Phys. 1991;70(2):988–92. https://doi.org/10.1063/1.349611
24. Pruneda JM, Artacho E. First-principles study of structural, elastic, and bonding properties of pyrochlores. Phys Rev B. 2005;72(8):085107. https://doi.org/10.1103/PhysRevB.72.085107
25. Ghosh S, Teweldebrhan D, Morales JR, Garay JE, Balandin AA. Thermal properties of the optically transparent pore-free nanostructured yttria-stabilized zirconia. J Appl Phys. 2009;106(11). https://doi.org/10.1063/1.3264613
26. Lebrun JM, Morrissey TG, Francis JSC, Seymour KC, Kriven WM, Raj R. Emergence and extinction of a new phase during on-off experiments related to flash sintering of 3YSZ. J Am Ceram Soc. 2015;98(5):1493–97. https://doi.org/10.1111/JACE.13476
27. Lebrun JM, Jha SK, McCormack SJ, Kriven WM, Raj R, Chan H. Broadening of diffraction peak widths and temperature

nonuniformity during flash experiments. J Am Ceram Soc. 2016;99(10):3429–34. https://doi.org/10.1111/JACE.14326
28. Lebrun JM, Hellberg CS, Jha SK, Kriven WM, Steveson AJ, Seymour KC, et al. In-situ measurements of lattice expansion related to defect generation during flash sintering. J Am Ceram Soc. 2017;100(11):4965–70. https://doi.org/10.1111/JACE.15071
29. Vikrant KSN, Wang H, Jana A, Wang H, García RE. Flash sintering incubation kinetics. NPJ Comput Mater. 2020;6(1):98. https://doi.org/10.1038/s41524-020-00359-7
30. Winn AJ, Todd RI. Microstructural requirements for alumina–SiC nanocomposites. Br Ceram Trans. 1999;98(5):219–24. https://doi.org/10.1179/096797899680471
31. Jiao S, Jenkins ML. A quantitative analysis of crack-interface interactions in alumina-based nanocomposites. Philos Mag A. 1998;78(2):507–22. https://doi.org/10.1080/01418619808241916
32. Parchovianský M, Galusek D, Sedláček J, Švančárek P, Kašiarová M, Dusza J, et al. Microstructure and mechanical properties of hot pressed Al2O3/SiC nanocomposites. J Eur Ceram Soc. 2013;33(12):2291–98. https://doi.org/10.1016/j.jeurceramsoc.2013.01.024
33. Harrison RW, Lee WE. Processing and properties of ZrC, ZrN and ZrCN ceramics: a review. Adv Appl Ceram. 2016;115(5):294–307. https://doi.org/10.1179/1743676115Y.0000000061
34. Lengauer W. Transition metal carbides, nitrides, and carbonitrides. In: Riedel R, editor. Handbook of ceramic hard materials. Wiley; 2000. p. 202–52. https://doi.org/10.1002/9783527618217.ch7
35. Li J, Cho J, Ding J, Charalambous H, Xue S, Wang H, et al. Nanoscale stacking fault-assisted room temperature plasticity in flash-sintered $TiO_2$. Sci Adv. 2019;5(9). https://doi.org/10.1126/sciadv.aaw5519
36. Sternlicht H, Rheinheimer W, Dunin-Borkowski RE, Hoffmann MJ, Kaplan WD. Characterization of grain boundary disconnections in $SrTiO_3$ part I: the dislocation component of grain boundary disconnections. J Mater Sci. 2019;54(5):3694–709. https://doi.org/10.1007/s10853-018-3096-4
37. Moura C, Carvalho P, Vaz F, Cunha L, Alves E. Raman spectra and structural analysis in ZrOxNy thin films. Thin Solid Films. 2006;515(3):1132–37. https://doi.org/10.1016/J.TSF.2006.07.039
38. Spengler W, Kaiser R. First and second order Raman scattering in transition metal compounds. Solid State Commun. 1976;18(7):881–84. https://doi.org/10.1016/0038-1098(76)90228-3
39. Spengler W, Kaiser R, Christensen AN, Müller-Vogt G. Raman scattering, superconductivity, and phonon density of states of stoichiometric and nonstoichiometric TiN. Phys Rev B. 1978;17(3):1095–101. https://doi.org/10.1103/PhysRevB.17.1095
40. Stoehr M, Seo H-S, Petrov I, Greene JE. Raman scattering from epitaxial HfN layers grown on MgO(001). J Appl Phys. 2006;99(4):043507. https://doi.org/10.1063/1.2173037
41. Tenne DA, Gönenli İE, Soukiassian A, Schlom DG, Nakhmanson S, Rabe KM, et al. Raman study of oxygen reduced and re-oxidized strontium titanate. Phys Rev B. 2007;76(2):024303. https://doi.org/10.1103/PhysRevB.76.024303
42. Fang Q, Blum L, Stolten D. Electrochemical performance and degradation analysis of an SOFC short stack following operation of more than 100,000 hours. J Electrochem Soc. 2019;166(16):F1320–25. https://doi.org/10.1149/2.0751916JES/XML
43. Menzler NH, Sebold D, Sohn YJ, Zischke S. Post-test characterization of a solid oxide fuel cell after more than 10 years of stack testing. J Power Sources. 2020;478:228770. https://doi.org/10.1016/j.jpowsour.2020.228770
44. Lang M, Bohn C, Henke M, Schiller G, Willich C, Hauler F. Understanding the current-voltage behavior of high temperature solid oxide fuel cell stacks. J Electrochem Soc. 2017;164(13):F1460–70. https://doi.org/10.1149/2.1541713jes

## SUPPORTING INFORMATION

Additional supporting information can be found online in the Supporting Information section at the end of this article.

**How to cite this article:** Bechteler C, Todd RI. Electrochemical reduction-induced phase transformation and lattice modification in cubic zirconia (8YSZ). Int J Appl Ceram Technol. 2025;e70011. https://doi.org/10.1111/ijac.70011